Geophysical Research Letters

RESEARCH LETTER
10.1029/2021GL095797

Special Section:
Southern Ocean and Climate: Biogeochemical and Physical Fluxes and Processes

Controls on the Boundary Between Thermally and Non-Thermally Driven pCO_2 Regimes in the South Pacific

Channing J. Prend[1], Jess M. Hunt[2], Matthew R. Mazloff[1], Sarah T. Gille[1], and Lynne D. Talley[1]

[1]Scripps Institution of Oceanography, University of California San Diego, La Jolla, CA, USA, [2]Department of Civil and Environmental Engineering, Princeton University, Princeton, NJ, USA

Key Points:

- Biogeochemical float data confirm that the leading driver of pCO_2 seasonality shifts with latitude in the southern subtropical gyre
- The boundary between pCO_2 regimes is primarily set by the poleward decrease in sea surface temperature (SST) seasonal cycle amplitude
- The reduction in SST seasonal cycle amplitude, in turn, is linked to the northern boundary of deep winter mixed layers

Supporting Information:

Supporting Information may be found in the online version of this article.

Correspondence to:

C. J. Prend,
cprend@ucsd.edu

Citation:

Prend, C. J., Hunt, J. M., Mazloff, M. R., Gille, S. T., & Talley, L. D. (2022). Controls on the boundary between thermally and non-thermally driven pCO_2 regimes in the South Pacific. *Geophysical Research Letters*, *49*, e2021GL095797. https://doi.org/10.1029/2021GL095797

Received 19 AUG 2021
Accepted 20 APR 2022

Abstract Regional and temporal patterns of air–sea carbon exchange are strongly linked to the surface ocean partial pressure of carbon dioxide (pCO_2), which varies with sea surface temperature (SST), salinity, dissolved inorganic carbon (DIC), and alkalinity. It is well-known that temperature controls the pCO_2 seasonal cycle in the subtropics, whereas DIC dominates at high latitudes. The balance of mechanisms governing the boundary between these regimes, however, are not well characterized due to lack of year-round pCO_2 data. Here, we use autonomous biogeochemical float measurements from the South Pacific to investigate the processes that control meridional variations in pCO_2 seasonality. We find that the transition between pCO_2 regimes is linked to the poleward decrease in SST seasonal cycle amplitude, which is closely associated with the northern boundary of deep winter mixed layers. Processes that determine the annual SST range are, therefore, central to the response of oceanic carbon uptake to anthropogenic forcing.

Plain Language Summary Air–sea carbon fluxes, which regulate the global climate system, vary seasonally and geographically, in large part due to variability in the surface ocean partial pressure of carbon dioxide (pCO_2). Surface pCO_2 variability can be separated into components due to changes in temperature and biology. The relative importance of these components varies regionally. In the subtropics, the pCO_2 seasonal cycle is controlled by temperature, while the non-thermal component dominates in polar regions. In this study, we examine what controls the location of the boundary between these two pCO_2 regimes. To do this, we use measurements from autonomous biogeochemical floats, which sample year round in the South Pacific, a region with limited historical measurements. We find that the transition between pCO_2 regimes is most closely related to the decrease in annual surface temperature range toward the south, where winter mixing is deep. This result can help diagnose biases in modeled air–sea carbon fluxes and indicate whether locations of oceanic carbon uptake will change in the future.

1. Introduction

The Southern Ocean, south of 30°S, constitutes a significant portion of the global oceanic carbon uptake, which regulates the climate system (Caldeira & Duffy, 2000; DeVries, 2014; Frölicher et al., 2015; Orr et al., 2001). Although the Southern Ocean is a net sink for atmospheric carbon dioxide (CO_2), air–sea carbon fluxes (F_{CO_2}) exhibit variability across a wide range of scales (Gruber et al., 2019; Ritter et al., 2017; Rödenbeck et al., 2015). F_{CO_2} (Figure S1 in Supporting Information S1) strength depends on the difference in partial pressure of CO_2 (pCO_2) between the ocean and atmosphere, the gas transfer velocity, and the solubility of CO_2 in seawater (Takahashi et al., 1997; Wanninkhof, 2014). The direction of the flux, however, is determined solely by the sign of the air–sea pCO_2 gradient. Given that spatio-temporal variability in surface ocean pCO_2 is much greater than that of atmospheric pCO_2, the oceanic pCO_2 determines seasonal and geographic variations in air–sea carbon exchange (Takahashi et al., 2002).

Surface ocean pCO_2 variability can be decomposed into components due to changes in sea surface temperature (SST), salinity, dissolved inorganic carbon (DIC), and total alkalinity (TA; Sarmiento & Gruber, 2006; Takahashi et al., 2014). The dominant mode of variability is the seasonal cycle, which is generally assumed to be controlled by the temperature and DIC components (Landschützer et al., 2018; Mongwe et al., 2018; Takahashi et al., 2002, 2014). The temperature (or "thermal") component of pCO_2 seasonality peaks in late summer when sea surface temperature (SST) is highest due to incoming solar radiation and air–sea heat fluxes. The "non-thermal" component of pCO_2 seasonality, in contrast, peaks in late winter when surface DIC is highest

due to respiration and entrainment of subsurface carbon during wintertime mixing (Landschützer et al., 2013; Takahashi et al., 1997, 2002).

Therefore, the seasonal cycle of pCO_2 at a given location depends on the relative magnitude of the thermal and non-thermal components, which are out of phase. For example, the subtropics are thermally driven, as evidenced by the strong correlation of pCO_2 with SST (Sutton et al., 2017; Takahashi et al., 2002), with pCO_2 high in winter and low in summer. In the subpolar and polar regions, on the other hand, pCO_2 is non-thermally driven and thus in phase with DIC changes (Fay et al., 2018; Williams et al., 2018). The transition between these two regimes in the Southern Hemisphere occurs in the southern subtropical gyre and is often attributed to a meridional gradient in the Revelle Factor (RF), which increases the sensitivity of pCO_2 to DIC variations at high latitudes (Fassbender et al., 2018; Takahashi et al., 2002). However, changes in the annual range of SST or DIC could also contribute to these patterns. While the latitudinal variation in the leading driver of pCO_2 seasonality has been well-documented (Landschützer et al., 2018; Takahashi et al., 2002, 2014; Williams et al., 2018), the processes controlling the position of the boundary between regimes have not been well characterized. This is likely due to the sparsity of year-round in situ biogeochemical measurements, which make it difficult to assess detailed spatial patterns of pCO_2 seasonality.

Until recently, the seasonal cycle of pCO_2 in the Southern Ocean was resolved at only a few locations (Fay et al., 2018; Munro et al., 2015). However, autonomous floats deployed south of 30°S by the Southern Ocean Carbon and Climate Observations and Modeling (SOCCOM) project have dramatically increased the regional distribution of year-round biogoechemical data (Talley et al., 2019), which can be used to estimate carbon system parameters (Williams et al., 2017, 2018). Here, we use measurements from 10 floats in the subtropical Pacific sector of the Southern Ocean to investigate the meridional shift in the leading driver of pCO_2 seasonality. Understanding what controls this transition point is necessary to improve climate models, which poorly represent the phasing of the pCO_2 seasonal cycle in the Southern Ocean (Anav et al., 2013; Mongwe et al., 2018). Furthermore, determining these mechanisms can help predict whether the distribution of pCO_2 regimes will change in the future, which would have implications for oceanic carbon uptake.

2. Data and Methods

In this study, we analyze biogeochemical data from SOCCOM floats, which measure temperature, salinity, dissolved oxygen, nitrate, pH, fluorescence and backscatter over the top 2,000 m of the water column (Johnson et al., 2017). The quality-controlled data from the 22 December 2020 SOCCOM snapshot are used here. (https://doi.org/10.6075/J0B27ST5), and all profiles are linearly interpolated onto a regular depth axis with 5 m vertical resolution. The SOCCOM snapshots include estimates of TA from a locally interpolated alkalinity regression (Carter et al., 2017), as well as pCO_2 and DIC derived from the alkalinity estimates and in situ pH (Williams et al., 2017). Here, we use data from 10 floats in the South Pacific (trajectories shown in Figure 1 and float IDs listed in Table S1 of Supporting Information S1) to investigate regional differences in pCO_2 seasonality. The float profiles are divided into thermally driven (TD; orange trajectories in Figure 1) and non-thermally driven (NTD; purple trajectories in Figure 1) regimes based on their position relative to the zero contour of winter minus summer mean surface ocean pCO_2 from the Landschützer climatology (Figure 1; further discussed in Section 3). The distribution of data by year and month is similar for both zones (Figures S2 and S3 in Supporting Information S1). We also use data from the full Argo array (Roemmich et al., 2019) up to 30 August 2020 to calculate mixed-layer depth (MLD) at individual profiles using a 0.03 kg m^{-3} density threshold (Dong et al., 2008); we then sort the profiles into 1° × 1° bins and find the maximum MLD in each bin.

In addition to the autonomous float measurements, we utilize monthly climatologies of pCO_2 and DIC from Landschützer et al. (2016) and Broullón et al. (2020), respectively. Both are observational data products that interpolate all available shipboard pCO_2 and DIC measurements onto 1° × 1° grids at monthly temporal resolution using feed-forward neural networks. We use Version 6.6 of the Landschützer pCO_2 climatology, which is based on Surface Ocean CO_2 Atlas (SOCAT) data from 1982 to 2021 (Bakker et al., 2016). The DIC climatology is derived from Global Ocean Data Analysis Project (GLODAP) and Lamont-Doherty Earth Observatory (LDEO) data from 1957 to 2019 (Olsen et al., 2019; Takahashi et al., 2017). We also use the NOAA Optimum Interpolation (OI) SST reanalysis, which combines satellite and in situ SST measurements (Reynolds & Smith, 1994). Here we

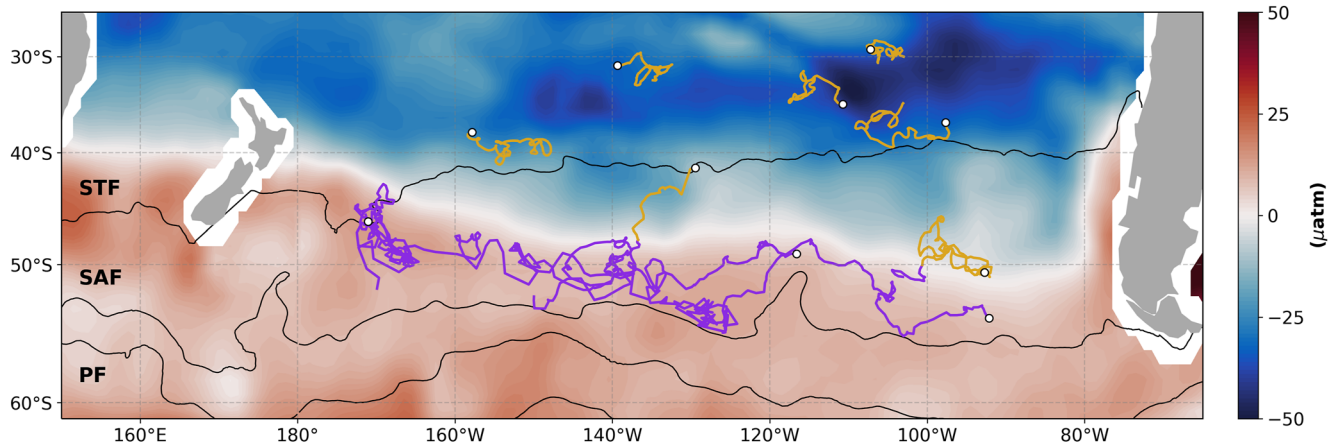

Figure 1. Autonomous float trajectories from the thermal (orange) and non-thermal (purple) regimes; the end of each float trajectory is marked with a circle. Shading denotes the winter (JJA) minus summer (DJF) mean surface ocean pCO_2 (μatm) from the Landschützer climatology. This quantity is positive (red) where pCO_2 is highest in winter, hence non-thermally driven, and negative (blue) where pCO_2 is lowest in winter, hence thermally driven. Black lines mark the Antarctic Circumpolar Current fronts (Gray et al., 2018), which are from north to south, the Subtropical Front (STF), Subantarctic Front (SAF), and Polar Front (PF).

use the monthly SST climatology at 1° × 1° resolution from OI Version 2.1, which incorporates data from 2002 to 2020 (Huang et al., 2021). Finally, we use the 1980–2000 mean surface Revelle Factor from Jiang et al. (2019).

For the TD and NTD regimes, we calculate climatological seasonal cycles of all measured and derived fields from the float data. Each profile is averaged over the top 20 m of the water column to represent the surface value, and climatologies are calculated at 10-day temporal resolution by linearly interpolating the profile data in time to common 10-day intervals and then averaging over each interval (Figure 2). We then decompose the pCO_2 seasonality into temperature, salinity, DIC, and alkalinity components (Sarmiento & Gruber, 2006; Takahashi et al., 2014). In this framework, the first-order terms of a Taylor expansion are used to relate changes in pCO_2 (δpCO_2) directly to changes in temperature (δT), salinity (δS), DIC (δDIC), and TA (δTA). This is only strictly valid for small perturbations.

$$\delta pCO_2 = \frac{\partial pCO_2}{\partial T}\delta T + \frac{\partial pCO_2}{\partial S}\delta S + \frac{\partial pCO_2}{\partial DIC}\delta DIC + \frac{\partial pCO_2}{\partial TA}\delta TA. \quad (1)$$

Since we are interested in the seasonal cycle, δpCO_2, δT, δS, δDIC, and δTA are taken to be deviations from the annual mean. Following Takahashi et al. (2014), we assume that the terms on the right-hand side of Equation 1 are approximated by

$$\frac{\partial pCO_2}{\partial T}\delta T = 2 \cdot \overline{pCO_2}\left(\exp\left(0.0423 \cdot \frac{\delta T}{2}\right) - 1\right), \quad (2)$$

$$\frac{\partial pCO_2}{\partial S}\delta S = 0.026 \cdot \overline{pCO_2}\delta S, \quad (3)$$

$$\frac{\partial pCO_2}{\partial DIC}\delta DIC = RF\left(\frac{\overline{pCO_2}}{\overline{DIC}}\right)\delta DIC, \quad (4)$$

$$\frac{\partial pCO_2}{\partial TA}\delta TA = \gamma\left(\frac{\overline{pCO_2}}{\overline{TA}}\right)\delta TA, \quad (5)$$

where the overbar denotes an annual mean. RF is the Revelle Factor, and γ is the buffer factor for alkalinity; both are evaluated from the float data using CO2SYS (Humphreys et al., 2020). Figure 3 shows the decomposition of the seasonal cycle for the TD and NTD regimes. The left-hand and right-hand sides of Equation 1, as calculated from the float climatologies, are not necessarily equal given that spatial and sub-seasonal variability may be aliased into the climatologies, and also that the Taylor expansion approximation is imperfect (Landschützer

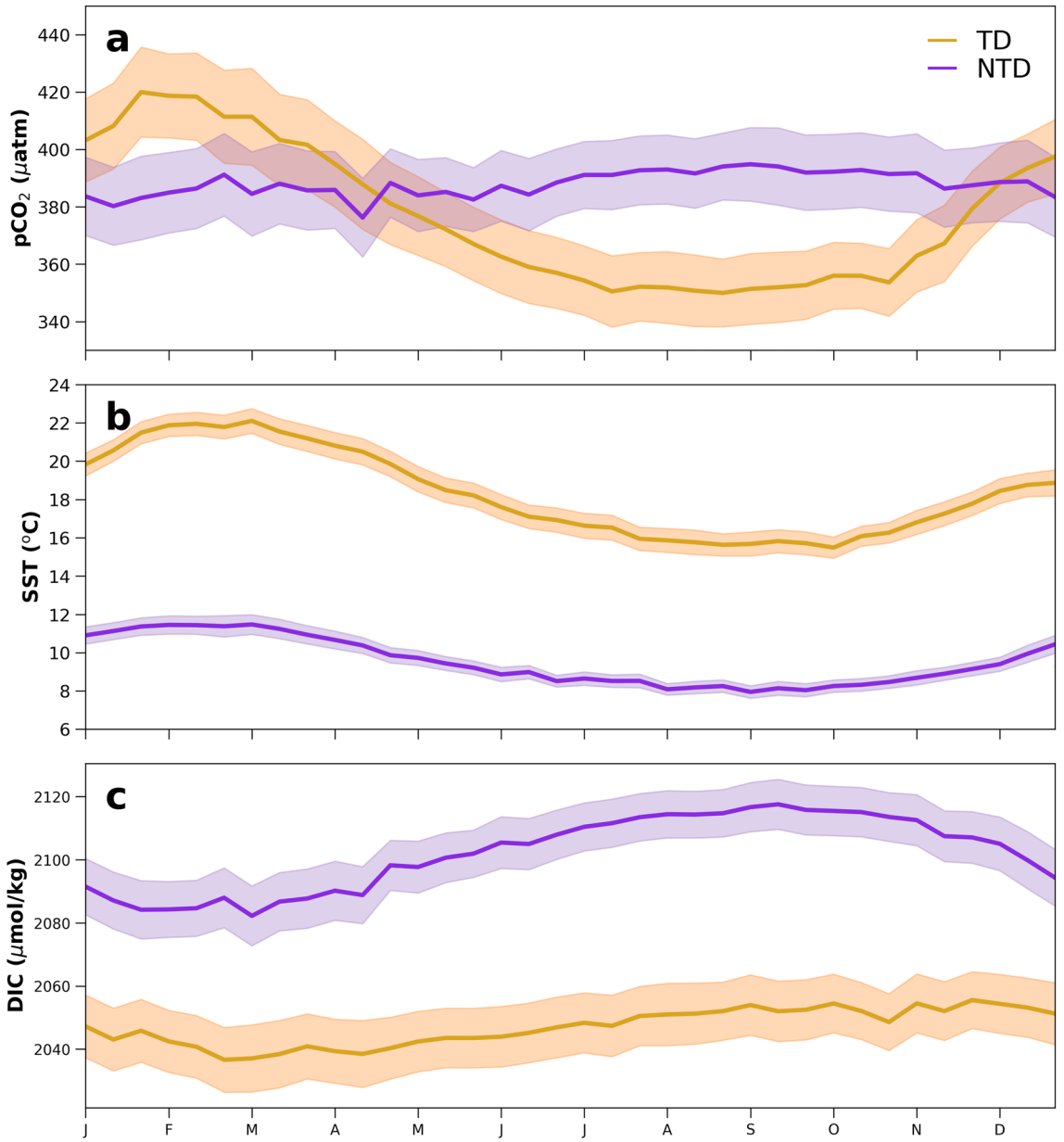

Figure 2. Autonomous float-derived climatologies of (a) surface ocean pCO_2 (μatm) (b) sea surface temperature (°C) and (c) surface dissolved inorganic carbon (μmol/kg) for the thermal (orange) and non-thermal (purple) regimes (see float trajectories in Figure 1). Error bars reflect the variability within the region (i.e., standard error of the mean) as well as the uncertainty associated with estimating carbon system parameters from in situ pH (~12 μatm), calculated following Williams et al. (2017). These two uncertainties are added in quadrature to give the error bars.

et al., 2018; Lovenduski et al., 2007). However, we find that the residuals are small for both the TD and NTD (dashed black lines in Figure 3).

3. Results

3.1. Float Analysis

The spatial distribution of thermally and non-thermally driven pCO_2 regimes can be visualized by plotting the difference between austral winter and summer mean surface pCO_2, which is shown in Figure 1 from the Landschützer climatology. This quantity is positive (red) to the south where pCO_2 peaks in winter (i.e., is non-thermally driven), and negative (blue) to the north where pCO_2 peaks in summer (i.e., is thermally driven). The

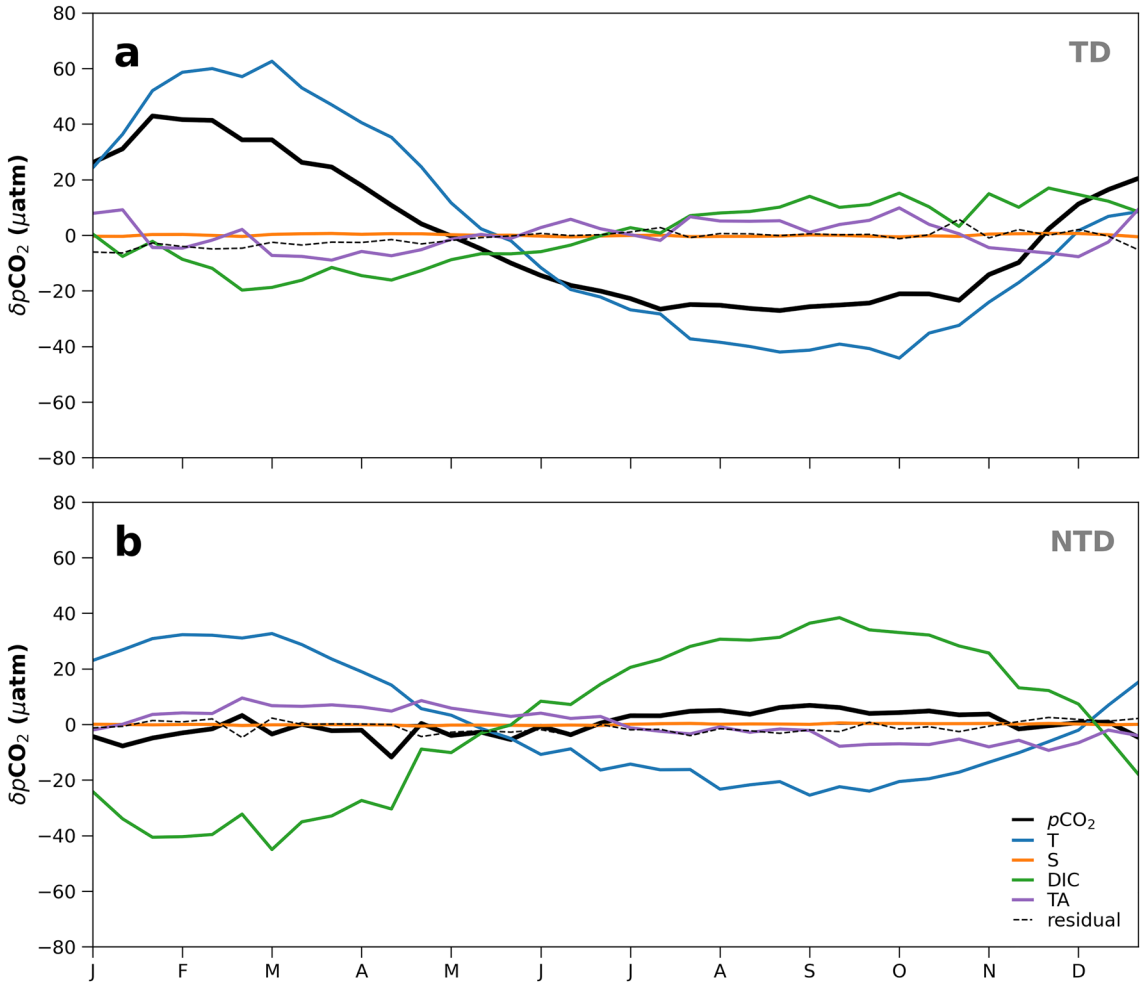

Figure 3. Decomposition of the pCO_2 seasonal cycle (black), expressed as a deviation from the annual mean, into components associated with variations in surface temperature (blue), salinity (orange), DIC (green), and TA (purple). The components are calculated from the float climatologies for the (a) thermal and (b) non-thermal regimes using Equations 1–5. Residuals are plotted as black dashed lines in each panel.

transition between regimes is marked by a narrow white region, around 45°S, where the pCO_2 seasonal cycle amplitude goes to zero. This transition is also evident from the 10 floats shown in Figure 1. Namely, float climatologies (Figure 2) show that surface pCO_2 is in phase with SST in the TD regime, signifying the temperature dominance of the seasonal cycle. In contrast, the pCO_2 amplitude is near-zero but slightly in phase with DIC in the NTD regime, reflecting the close proximity of the floats to the transition point (Figure 1).

The distinct pCO_2 seasonal cycle in the TD and NTD zones corresponds to differences in the mean and annual range of SST and DIC (Figures 2b and 2c), as well as RF (Table S2 in Supporting Information S1). In order to systematically assess the impact of these differences on the observed pCO_2 variability, we decompose the pCO_2 seasonal cycles using Equations 1–5 (Figure 3). The pCO_2 changes associated with salinity and TA are similar between both regimes and small in amplitude relative to the SST and DIC components. For example, the seasonal cycle amplitude of the salinity component is at most 1.7% of the SST component and 17.6% of the DIC component in the TD and NTD. Therefore, the relative importance of thermal and non-thermal drivers is quantified by taking the ratio of the amplitudes of the temperature (Equation 2) and DIC (Equation 4) components, henceforth referred to as *S*/*D* (for "SST"/"DIC"); Takahashi et al. (2002) called this ratio *T*/*B* (for "temperature"/"biology"), however here we adopt the notation *S*/*D* to acknowledge that surface DIC is altered by both biological *and* physical processes. Note that *S*/*D* does not explicitly contain any phase information; however, if we assume that the temperature and DIC components are exactly out of phase, pCO_2 is thermally driven when $S/D > 1$ and non-thermally driven when $S/D < 1$. The boundary between regimes occurs when the components perfectly compensate,

i.e. $S/D = 1$. While SST and DIC are not necessarily exactly out of phase, this is a reasonable approximation for the data considered here (Figures 2b and 2c), and thus, the S/D value can be interpreted without considering phase offsets. Based on the float climatologies, S/D is 3.04 in the northern subtropics, as expected for the TD regime. In the southern subtropics, S/D is 0.71, reflecting the slight dominance of the DIC component and consistent with the NTD regime; the closeness to 1 signifies the much smaller pCO_2 seasonal cycle amplitude. This difference in S/D between regimes is due to changes in the amplitude of both the temperature and DIC components, as shown next.

Several possible factors could lead to the meridional gradient in S/D, including changes in RF in addition to the seasonal cycle amplitudes of SST and/or DIC. Therefore, to understand the dominant driver, we must consider the magnitude of annual SST and DIC variations as well as the local chemical conditions (i.e., mean pCO_2 and buffering capacity). The thermal component is a function of both the annual SST range and the annual mean pCO_2 value (Equation 2). Regions with the same SST seasonal cycle but different mean pCO_2 values will respond to temperature perturbations with different amplitude pCO_2 changes. This effect, however, is minimal when comparing the TD and NTD, which have similar mean pCO_2 (Table S2 in Supporting Information S1). Therefore, the smaller amplitude thermal component in the NTD regime must be solely due to the smaller annual SST range. Moving from the TD to the NTD, the SST seasonal cycle amplitude decreases by 48%; this corresponds to a 50% decrease of S/D due solely to the change in δSST. In fact, the NTD would be thermally driven if it had the same annual SST range as the TD, leaving all other variables unchanged.

The DIC component, in turn, depends on both the annual DIC range as well as RF (Equation 4). RF is larger in the polar regions, due to cold temperatures and upwelling of deep waters with high DIC/TA, which means that pCO_2 is more sensitive to DIC perturbations (Fassbender et al., 2017; Jiang et al., 2019); this effect helps explain the dominance of the non-thermal component of pCO_2 at high latitudes (Fassbender et al., 2018; Takahashi et al., 2002). However, the float data suggest that spatial differences in RF alone do not explain the exact position of the boundary between pCO_2 regimes. Moving from the TD to the NTD, RF increases by 21%; this corresponds to an 18% decrease of S/D due solely to the change in RF. This decrease in S/D is not large enough on its own to account for the change in pCO_2 seasonal cycle phasing between the TD and NTD, which would require a 39% increase in RF to produce the observed difference. In addition to RF, the regimes also have distinct differences in DIC seasonal cycle amplitude. Namely, the annual DIC range increases by 52% from the TD to the NTD, which corresponds to a 44% decrease of S/D due solely to the change in the magnitude of the DIC seasonal cycle.

3.2. Gridded Products

We place these results in a larger-scale regional context by using satellite and in situ data products. Figures 4a and 4b shows the annual SST range and annual mean pCO_2, which together determine the amplitude of the temperature component of pCO_2. Figures 4c and 4d then shows the annual surface DIC range and annual mean RF, which together determine the amplitude of the DIC component of pCO_2. Finally, Figure 4g shows the ratio S/D derived from the gridded climatologies. δSST decreases toward the south (Figure 4a), which is related to the annual range of net surface heat flux and MLD distribution (Chiodi & Harrison, 2010). RF, in contrast, increases poleward (Figure 4d) due to colder temperatures, as well as unutilized macronutrients and upwelling of high DIC/TA waters in the Antarctic Circumpolar Current (ACC; Egleston et al., 2010; Sabine et al., 2004). Both of these factors favor a thermally driven pCO_2 seasonal cycle in the subtropics and a non-thermally driven pCO_2 seasonal cycle at high latitudes. However, the precise location of the boundary between pCO_2 regimes (dashed white line in Figure 4) corresponds to a sharp decrease in δSST, whereas RF increases linearly with latitude across the whole Southern Ocean (Figures 4e and 4f).

The nearly 50% decrease in annual SST range coincides with a significant deepening of the maximum winter mixed-layer depth toward the south (Figure 5a). This is expected because deep MLDs in the Subantarctic Zone (SAZ)—between the Subtropical and Subantarctic Fronts—increase the volume of the mixed-layer, which makes SST less responsive to atmospheric forcing, and thus damps δSST (Chiodi & Harrison, 2010). Furthermore, there is a tight correspondence between the pCO_2 regime boundary and a front that marks the northern edge of deep winter mixed layers in the SAZ (Figure 5b). Zonal variations in both fields mirror each other almost exactly. They also align with the border between the Fay and McKinley (2014) subtropical seasonally stratified and subtropical permanently stratified biomes. Their bioregion definitions were based on SST, surface chlorophyll, and MLD,

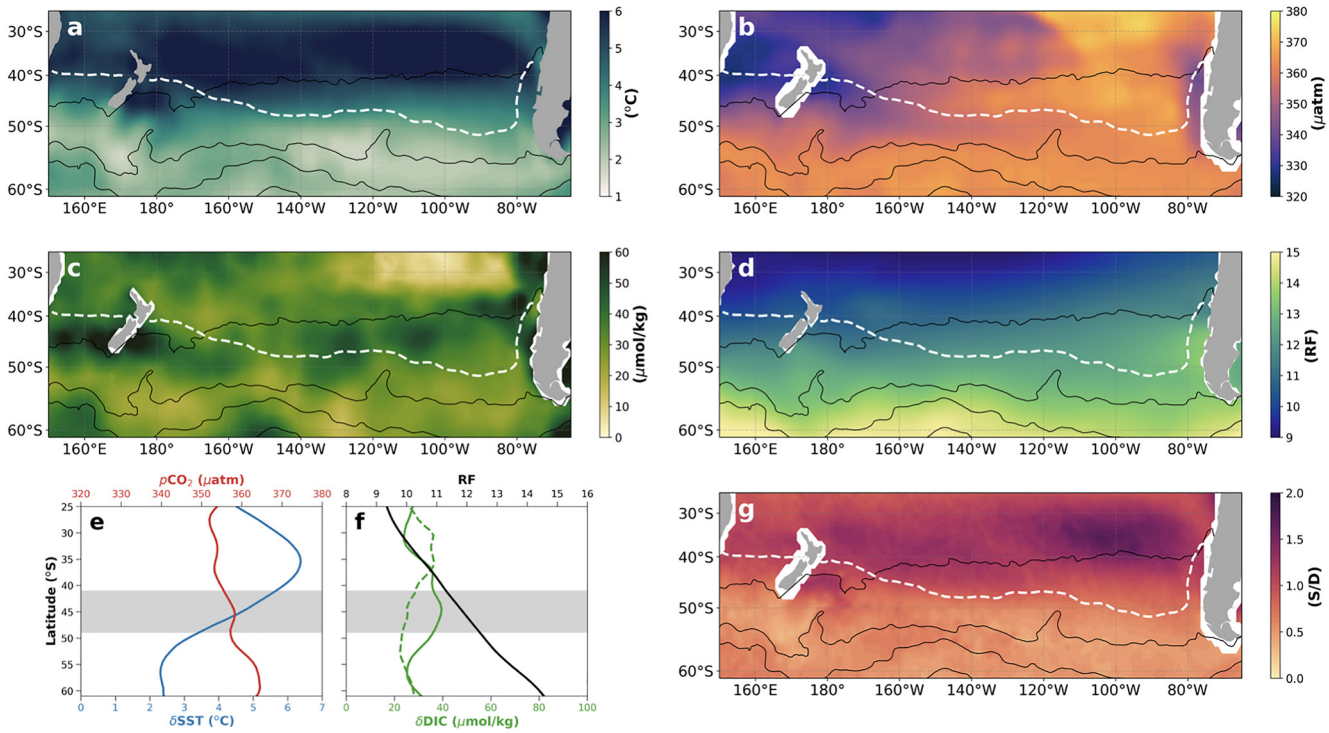

Figure 4. (a) SST seasonal cycle amplitude (°C) from the NOAA OI monthly SST climatology; (b) annual mean surface ocean pCO_2 (μatm) from the Landschützer climatology; (c) surface DIC seasonal cycle amplitude (μmol/kg) from the Broullón et al. (2020) monthly DIC climatology; (d) 1980–2000 mean surface Revelle Factor from Jiang et al. (2019); (g) The ratio of thermal to DIC component amplitudes (*S*/*D*) derived from the gridded products. In each of these panels, black lines denote the ACC fronts. The dashed white line is the approximate boundary between pCO_2 regimes, inferred as the zero contour of JJA-DJF mean surface ocean pCO_2 (Figure 1) from the Landschützer climatology. (e) SST seasonal cycle amplitude (°C) from the NOAA OI monthly SST climatology and annual mean surface ocean pCO_2 (μatm) from the Landschützer climatology, (f) surface DIC seasonal cycle amplitude (μmol/kg) from the Broullón et al. (2020) monthly DIC climatology (solid) and from the Keppler et al. (2020) monthly DIC climatology (dashed), and 1980–2000 mean surface Revelle Factor from Jiang et al. (2019). All quantities in (e) and (f) are zonally averaged over the Pacific (160°E to 80°W). Gray shading in these panels mark the approximate latitude range of the pCO_2 regime boundary in the Pacific.

but not pCO_2. This points to the overall importance of MLD in determining not only the pCO_2 regime boundary but also biogeography.

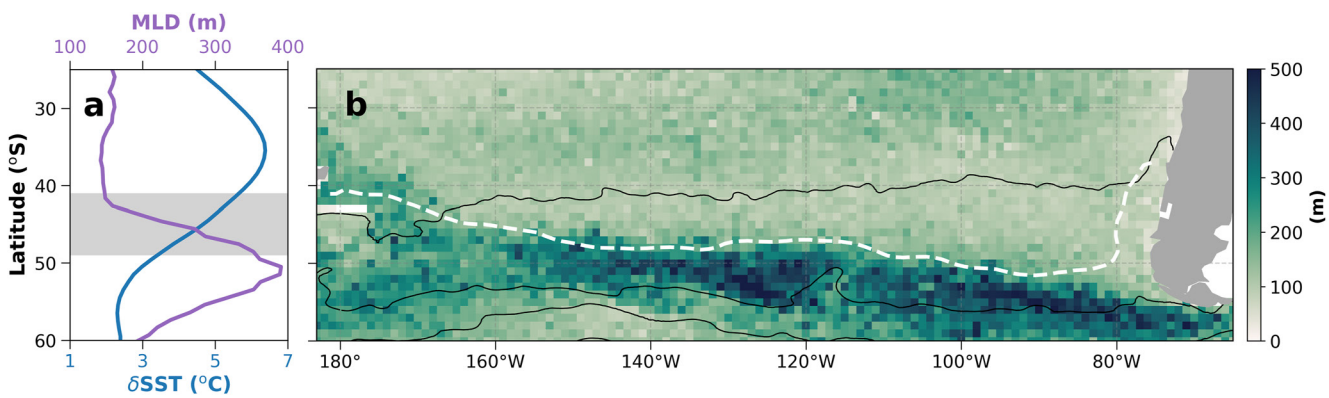

Figure 5. (a) SST seasonal cycle amplitude (°C) from the NOAA OI monthly SST climatology (blue) and maximum winter MLD (m) from Argo data (purple). Both quantities are zonally averaged over the Pacific (160°E to 80°W). Gray shading marks the approximate latitude range of the pCO_2 regime boundary in the Pacific. (b) Maximum winter MLD (m) in 1° × 1° bins from Argo data, 2000–2020. Black lines mark the Antarctic Circumpolar Current fronts (Gray et al., 2018). The dashed white line is the approximate boundary between pCO_2 regimes, inferred as the zero contour of JJA-DJF mean surface ocean pCO_2 (Figure 1) from the Landschützer climatology.

The float data suggest that δDIC also contributes to the difference in pCO_2 seasonality between the TD and NTD, which could be related to increased biological productivity in the great calcite belt compared with the oligotrophic gyre (Balch et al., 2016). However, the annual DIC range from the Broullón et al. (2020) product does not exhibit a strong meridional gradient (Figures 4c and 4f). This may be due to sampling bias by the floats, since subsampling the Broullón et al. (2020) product at the float profile locations increases the difference in δDIC between frontal zones (not shown). It is also possible that seasonal biases in the shipboard data used to train the Broullón et al. (2020) neural network lead to an underestimate of δDIC at high latitudes. However, a different DIC product that incorporates year-round SOCCOM float data (Keppler et al., 2020) also shows a weak meridional gradient in δDIC at the pCO_2 regime boundary (Figure 4f). In other words, δDIC does not appear to control the position of the regime boundary, despite its correspondence to the location of the great calcite belt (Figure S4c in Supporting Information S1) as inferred from satellite estimates of particulate inorganic carbon (Balch et al., 2005).

4. Discussion

Surface ocean pCO_2 exerts control over spatial and temporal patterns of air–sea carbon exchange. Therefore, untangling the drivers of pCO_2 variability has important implications for global climate. The phasing of the pCO_2 seasonal cycle exhibits significant regional differences. It has long been known that pCO_2 is thermally driven in the subtropics and non-thermally driven at high latitudes (Landschützer et al., 2016; Takahashi et al., 2002, 2014; Williams et al., 2018). The mechanisms controlling this shift could include the lower buffering capacity of seawater in the polar regions (Fassbender et al., 2018; Takahashi et al., 2002), the southward increase in biological productivity associated with the great calcite belt (Balch et al., 2005), meridional variations in wintertime entrainment of DIC, and changes in the SST seasonal cycle amplitude. Here, we have shown that the precise boundary between thermally and non-thermally driven pCO_2 regimes in the South Pacific is most strongly related to the poleward decrease in annual SST range, which is primarily tied to the MLD distribution. Namely, the transition occurs within the SAZ and is aligned with a front along the north side of the deep winter mixed layers ("Mode Water" formation region) in the southern subtropical gyre.

These results stem from new autonomous biogeochemical float measurements, which fully resolve the pCO_2 seasonal cycle in locations with limited year-round historical measurements. We separated float profiles into TD and NTD regimes, and decomposed the pCO_2 variability into components due to temperature, salinity, DIC, and TA variations. We found that the transition between pCO_2 regimes corresponds to changes in the amplitude of both the temperature and DIC components. The amplitude of the temperature component is 55 μatm smaller in the NTD compared to the TD, which is due entirely to differences in the annual SST range. Meanwhile the amplitude of the DIC component is 44 μatm larger in the NTD due to both a higher RF and larger annual DIC range. While our focus here is on the South Pacific, the results may also be applicable to other basins; the transition between pCO_2 regimes occurs further to the north in the South Atlantic and Indian Oceans, but still appears to be related to the annual SST range and maximum winter MLD (Figure S4 in Supporting Information S1).

Isolating the components of pCO_2 variability is relevant to climate models, which often do not capture the correct phasing of the pCO_2 seasonal cycle in the Southern Ocean (Anav et al., 2013; Mongwe et al., 2018). Namely, the models show peak pCO_2 in summer in the Southern Ocean, which does not match observations (Fay & McKinley, 2021). The discrepancy arises from the boundary between pCO_2 regimes being too far south in the models. Our findings imply that representing the annual SST range is crucial to modeling regional patterns of pCO_2 seasonality. This is consistent with results from Mongwe et al. (2018), who found that many CMIP5 models have an exaggerated SST seasonal cycle amplitude, resulting in biases in the seasonal cycle of pCO_2 and F_{CO_2}. Furthermore, Mongwe et al. (2018) showed that even models with realistic pCO_2 seasonal cycles often still had SST biases that were compensated for by excessive DIC changes associated with higher than observed primary productivity. Together with our results, this suggests that accurately reproducing the magnitude of seasonal SST changes is a prerequisite to better representation of air–sea carbon fluxes in climate models. Moreover, capturing the annual SST range likely requires improving model MLDs, which are known to be poorly represented in the Southern Ocean in many CMIP models (Sallée et al., 2013).

In addition to the ramifications for modeling, understanding what controls the transition point between pCO_2 regimes is necessary to predict future changes. There is already observational evidence that the pCO_2 seasonal cycle is amplifying due to anthropogenic carbon uptake (Landschützer et al., 2018), which increases the mean

surface ocean pCO_2 (making pCO_2 more sensitive to temperature perturbations) and decreases the buffering capacity (making pCO_2 more sensitive to DIC perturbations). It has also been shown that changes in RF under RCP8.5 forcing drive an asymmetric amplification of the pCO_2 seasonal cycle (Fassbender et al., 2018). In addition to these mechanisms, which are solely associated with the response of seawater chemistry to increasing atmospheric CO_2, changes in stratification and primary productivity could impact the annual ranges of sea surface temperature, salinity, DIC, and TA (Behrenfeld et al., 2006; Boyce et al., 2010; Capotondi et al., 2012; Chavez et al., 2011; Li et al., 2020; Sallée et al., 2021). Indeed, predicting future changes in pCO_2 seasonality is difficult given the complex dependence on chemical, physical, and biological processes. Still, our results suggest that the SST seasonal cycle amplitude plays a leading order role in determining the distribution of thermally and non-thermally driven pCO_2 regimes, and thus deserves further examination in regard to modeled F_{CO_2} biases and the impact of climate change on the carbon cycle.

5. Summary and Conclusions

Spatial patterns of surface ocean pCO_2 seasonality greatly influence oceanic carbon uptake. Previous analyses of shipboard data have showed a meridional gradient in the leading driver of the pCO_2 seasonal cycle (Landschützer et al., 2013, 2018; Takahashi et al., 2002, 2014). Namely, pCO_2 is thermally driven in the subtropics and non-thermally driven at high latitudes (Landschützer et al., 2018; Takahashi et al., 2014; Williams et al., 2018). The boundary between these regimes could result from differences in the buffering capacity of seawater, or in the size of annual SST or DIC fluctuations, which in turn could be due to multiple mechanisms. In this study, we use new autonomous float measurements to demonstrate that the dominant driver of the regime boundary is the SST seasonal cycle amplitude, which is closely related to the spatial pattern of MLD. Understanding the precise processes that control this boundary is crucial in order to improve model biases, and here we have found that accurate representation of the SST seasonal cycle is necessary to reproduce the observed pCO_2 variability. Future work should investigate how this mechanism modulates the pCO_2 and F_{CO_2} response to anthropogenic forcing.

Data Availability Statement

The quality-controlled data from the 22 December 2020 SOCCOM snapshot are used in this analysis (http://doi.org/10.6075/J0B27ST5). We also utilize the monthly pCO_2 climatology evolved from Landschützer et al. (2016) Version 6.6 using data through 2021 (http://www.nodc.noaa.gov/archive/arc0105/0160558/3.3/data/0-data/), the monthly DIC climatology from Broullón et al. (2020) (http://doi.org/10.20350/digitalCSIC/10551), the NOAA Optimum Interpolated monthly SST climatology from OI Version 2.1 (http://psl.noaa.gov/data/gridded/data.noaa.oisst.v2.html), and the 1980–2000 mean surface RF from Jiang et al. (2019) (http://doi.org/10.25921/kgqr-9h49).

Acknowledgments
CJP, MRM, STG, and LDT were supported by NSF PLR-1425989 and OPP-1936222. CJP was also supported by a National Science Foundation Graduate Research Fellowship under Grant No. DGE-1650112. JMH was supported by the High Meadows Environmental Institute Internship Program. Profiling float data were collected and made freely available by the Southern Ocean Carbon and Climate Observations and Modeling (SOCCOM) Project funded by the National Science Foundation, Division of Polar Programs (NSF PLR-1425989), supplemented by NASA (NNX14AP49B), and by Argo and the NOAA programs that contribute to it.

References

Anav, A., Friedlingstein, P., Kidston, M., Bopp, L., Ciais, P., Cox, P., & Zhu, Z. (2013). Evaluating the land and ocean components of the global carbon cycle in the CMIP5 earth system models. *Journal of Climate*, *26*, 6801–6843.

Bakker, D. C. E., Pfeil, B., Smith, K., Hankin, S., Olsen, A., Alin, S. R., & Watson, A. J. (2016). An update to the Surface Ocean CO_2 Atlas (SOCAT version 2). *Earth System Science Data*, *6*, 69–90.

Balch, W. M., Bates, N. R., Lam, P. J., Twining, B. S., Rosengard, S. Z., Bowler, B. C., & Rauschenberg, S. (2016). Factors regulating the Great Calcite Belt in the Southern Ocean and its biogeochemical significance. *Global Biogeochemical Cycles*, *30*, 1124–1144.

Balch, W. M., Gordon, H. R., Bowler, B. C., Drapeau, D. T., & Booth, E. S. (2005). Calcium carbonate measurements in the surface global ocean based on Moderate-Resolution Imaging Spectroradiometer data. *Journal of Geophysical Research: Oceans*, *110*, C07001.

Behrenfeld, M. J., O'Malley, R. T., Siegal, D. A., McClain, C. R., Sarmiento, J. L., Feldman, G. C., & Boss, E. S. (2006). Climate-driven trends in contemporary ocean productivity. *Nature*, *444*, 752–755.

Boyce, D. G., Lewis, M. R., & Worm, B. (2010). Global phytoplankton decline over the past century. *Nature*, *466*, 591–596.

Broullón, D., Pérez, F. F., Velo, A., Hoppema, M., Olsen, A., Takahashi, T., & Kozyr, A. (2020). A global monthly climatology of oceanic total dissolved inorganic carbon: A neural network approach. *Earth System Science Data*, *12*, 1725–1743.

Caldeira, K., & Duffy, P. B. (2000). The role of the Southern Ocean in uptake and storage of anthropogenic carbon dioxide. *Science*, *287*, 620–622.

Capotondi, A., Alexander, M. A., Bond, N. A., Curchitser, E. N., & Scott, J. D. (2012). Enhanced upper ocean stratification with climate change in CMIP3 models. *Journal of Geophysical Research: Oceans*, *117*, 591–596.

Carter, B. R., Feely, R. A., Williams, N. L., Dickson, A. G., Fong, M. B., & Takeshita, Y. (2017). Updated methods for global locally interpolated estimation of alkalinity, pH, and nitrate. *Limnology and Oceanography: Methods*, *16*, 119–131.

Chavez, F. P., Messié, M., & Pennington, J. T. (2011). Marine primary production in relation to climate variability and change. *Annual Review of Marine Science*, *3*, 227–260.

Chiodi, A. M., & Harrison, D. E. (2010). The annual range of Southern Hemisphere SST: Comparison with surface heat and possible reasons for the high-latitude falloff. *Journal of Climate*, *305*, 367–371.
DeVries, T. (2014). The oceanic anthropogenic CO_2 sink: Storage, air-sea fluxes, and transports over the industrial era. *Global Biogeochemical Cycles*, *28*, 631–647.
Dong, S., Sprintall, J., Gille, S. T., & Talley, L. D. (2008). Southern Ocean mixed-layer depth from Argo float profiles. *Journal of Geophysical Research: Oceans*, *113*, C06013.
Egleston, E. S., Sabine, C. L., & More, F. M. M. (2010). Revelle revisited: Buffer factors that quantify the response of ocean chemistry to changes in DIC and alkalinity. *Global Biogeochemical Cycles*, *24*, GB1002.
Fassbender, A. J., Rodgers, K. B., Palevsky, H. I., & Sabine, C. L. (2018). Seasonal asymmetry in the evolution of surface ocean pCO_2 and pH thermodynamic drivers and the influence on sea-air CO_2 flux. *Global Biogeochemical Cycles*, *32*, 1476–1497.
Fassbender, A. J., Sabine, C. L., & Palevsky, H. I. (2017). Nonuniform ocean acidification and attenuation of the ocean carbon sink. *Geophysical Research Letters*, *44*, 8404–8413.
Fay, A. R., Lovenduski, N. S., McKinley, G. A., Munro, D. R., Sweeney, C., Gray, A. R., & Williams, N. (2018). Utilizing the Drake Passage time-series to understand variability and change in subpolar Southern Ocean pCO_2. *Biogeosciences*, *15*, 3841–3855.
Fay, A. R., & McKinley, G. A. (2014). Global open-ocean biomes: Mean and temporal variability. *Earth System Science Data*, *6*, 273–284.
Fay, A. R., & McKinley, G. A. (2021). Observed regional fluxes to constrain modeled estimates of the ocean carbon sink. *Geophysical Research Letters*, *48*, e2021GL095325.
Frölicher, T. L., Sarmiento, J. L., Paynter, D. J., Dunne, J. P., Krasting, J. P., & Winton, M. (2015). Dominance of the Southern Ocean in anthropogenic carbon and heat uptake in CMIP5 models. *Journal of Climate*, *28*, 862–886. https://doi.org/10.1175/JCLI-D-14-00117.1
Gray, A. R., Johnson, K. S., Bushinsky, S. M., Riser, S. C., Russell, J. L., Talley, L. D., & Sarmiento, J. L. (2018). Autonomous biogeochemical floats detect significant carbon dioxide outgassing in the high-latitude Southern Ocean. *Geophysical Research Letters*, *45*, 9049–9057. https://doi.org/10.1029/2018GL078013
Gruber, N., Landschützer, P., & Lovenduski, N. S. (2019). The variable Southern Ocean carbon sink. *Annual Review of Marine Science*, *11*, 159–186. https://doi.org/10.1146/annurev-marine-121916-063407
Huang, B., Liu, C., Banzon, V., Freeman, E., Garrett, G., Hankins, B., & Zhang, H.-M. (2021). Improvements of the Daily Optimum Interpolation Sea Surface Temperature (DOISST) Version 2.1. *Journal of Climate*, *34*, 2923–2939.
Humphreys, M. P., Gregor, L., Pierrot, D., vanHeuven, S. M. A. C., Lewis, E. R., & Wallace, D. W. R. (2020). PyCO2SYS: Marine carbonate system calculations in Python. *Zenodo*. https://doi.org/10.5281/zenodo.3744275
Jiang, L.-Q., Carter, B. R., Feely, R. A., Lauvset, S. K., & Olsen, A. (2019). Surface ocean pH and buffer capacity: Past, present, and future. *Scientific Reports*, *9*, 18624.
Johnson, K. S., Plant, J. N., Coletti, L. J., Jannasch, H. W., Sakamoto, C. M., Riser, S. C., & Sarmiento, J. L. (2017). Biogeochemical sensor performance in the SOCCOM profiling float array. *Journal of Geophysical Research: Oceans*, *122*, 6416–6436.
Keppler, L., Landschützer, P., Gruber, N., Lauvset, S. K., & Stemmler, I. (2020). Seasonal carbon dynamics in the near-global ocean. *Global Biogeochemical Cycles*, *34*, e2020GB006571.
Landschützer, P., Gruber, N., & Bakker, D. C. E. (2016). Decadal variations and trends of the global ocean carbon sink. *Global Biogeochemical Cycles*, *30*, 1396–1417.
Landschützer, P., Gruber, N., Bakker, D. C. E., Schuster, U., Nakaoka, S., Payne, M. R., & Zeng, J. (2013). A neural network-based estimate of the seasonal to inter-annual variability of the Atlantic Ocean carbon sink. *Biogeosciences*, *10*, 7793–7815.
Landschützer, P., Gruber, N., Bakker, D. C. E., Stemmler, I., & Six, K. D. (2018). Strengthening seasonal marine CO_2 variations due to increasing atmospheric CO_2. *Nature Climate Change*, *8*, 146–150.
Li, G., Cheng, L., Zhu, J., Trenberth, K. E., Mann, M. E., & Abraham, J. P. (2020). Increasing ocean stratification over the past half-century. *Nature Climate Change*, *10*, 1116–1123.
Lovenduski, N. S., Gruber, N., Doney, S. C., & Lima, I. D. (2007). Enhanced CO_2 outgassing in the Southern Ocean from a positive phase of the Southern Annular Mode. *Global Biogeochemical Cycles*, *21*, GB2026.
Mongwe, N. P., Vichi, M., & Monteiro, P. M. S. (2018). The seasonal cycle of pCO_2 and CO_2 fluxes in the Southern Ocean: Diagnosing anomalies in CMIP5 Earth system models. *Biogeosciences*, *15*, 2851–2872.
Munro, D. R., Lovenduski, N. S., Stephens, B. B., Newberger, T., Arrigo, K. R., Takahashi, T., & Sweeney, C. (2015). Estimates of net community production in the Southern Ocean determined from time series observations (2002-2011) of nutrients, dissolved inorganic carbon, and surface ocean pCO_2 in Drake Passage. *Deep-Sea Research II*, *114*, 49–63.
Olsen, A., Lange, N., Key, R. M., Tanhua, T., Alvarez, M., Becker, S., & Wanninkhof, R. (2019). GLODAPv2.2019 – An update of GLODAPv2. *Earth System Science Data*, *11*, 1437–1451.
Orr, J. C., Maier-Reimer, E., Mikolajewicz, U., Monfray, P., Sarmiento, J. L., Toggweiler, J. R., & Boutin, J. (2001). Estimates of anthropogenic carbon uptake from four three-dimensional global ocean models. *Global Biogeochemical Cycles*, *15*, 43–60.
Reynolds, R. W., & Smith, T. M. (1994). Improved global sea surface temperature analyses. *Journal of Climate*, *7*, 929–948.
Ritter, R., Landschützer, P., Gruber, N., Fay, A. R., Iida, Y., Jones, S., & Zeng, J. (2017). Observation-based trends of the Southern Ocean carbon sink. *Geophysical Research Letters*, *44*, 12339–12348.
Rödenbeck, C., Bakker, D. C. E., Gruber, N., Iida, Y., Jacobson, A. R., Jones, S., & Zeng, J. (2015). Data-based estimates of the ocean carbon sink variability – First results of the Surface Ocean pCO_2 Mapping intercomparison (SOCOM). *Biogeosciences*, *12*, 7251–7278.
Roemmich, D., Alford, M. H., Claustre, H., Johnson, K., King, B., Moum, J., & Yasuda, I. (2019). On the future of Argo: A global, full-depth, multi-disciplinary array. *Frontiers in Marine Science*, *6*, 439.
Sabine, C. L., Feely, R. A., Gruber, N., Key, R. M., Lee, K., Bullister, J. L., & Rios, A. F. (2004). The oceanic sink for anthropogenic CO_2. *Science*, *305*, 367–371.
Sallée, J.-B., Pellichero, V., Akhoudas, C., Pauthenet, E., Vignes, L., Schmidtko, S., & Kuusela, M. (2021). Summertime increases in upper-ocean stratification and mixed-layer depth. *Nature*, *591*, 592–598.
Sallée, J.-B., Shuckburgh, E., Bruneau, A., Meijers, A. J. S., Bracegirdle, T. J., & Wang, Z. (2013). Assessment of Southern Ocean mixed-layer depths in CMIP5 models: Historical bias and forcing response. *Journal of Geophysical Research: Oceans*, *118*, 1845–1862.
Sarmiento, J. L., & Gruber, N. (2006). *Ocean Biogeochemical Dynamics*. Princeton University Press.
Sutton, A. J., Wanninkhof, R., Sabine, C. L., Feely, R. A., Cronin, M. F., & Weller, R. A. (2017). Variability and trends in surface seawater pCO_2 and CO_2 flux in the Pacific Ocean. *Geophysical Research Letters*, *44*, 5627–5636.
Takahashi, T., Feely, R. A., Weiss, R. F., Wanninkhof, R. H., Chipman, D. W., Sutherland, S. C., & Takahashi, T. T. (1997). Global air-sea flux of CO_2: An estimate based on measurements of sea-air pCO_2 difference. *Proceedings of the National Academy of Sciences*, *94*, 8292–8299.

Takahashi, T., Sutherland, S. C., Chipman, D. W., Goddard, J. G., Ho, C., Newberger, T., & Munro, D. R. (2014). Climatological distributions of pH, pCO_2, total CO_2, alkalinity, and $CaCO_3$ saturation in the global Surface Ocean, and temporal changes at selected locations. *Marine Chemistry*, *164*, 95–125.

Takahashi, T., Sutherland, S. C., & Kozyr, A. (2017). *Global Ocean Surface Water Partial Pressure of CO_2 Database: Measurements Performed During 1957-2016 (Version 2016) (Tech. Rep. No. NOAA/NCEI/OCADSNDP-088(V2016))*. Carbon Dioxide Information Analysis Center Oak Ridge National Laboratory, US Department of Energy.

Takahashi, T., Sutherland, S. C., Sweeney, C., Poisson, A., Metzl, N., Tilbrook, B., & Nojiri, Y. (2002). Global sea-air CO_2 flux based on climatological surface ocean pCO_2, and seasonal biological and temperature effects. *Deep-Sea Research II*, *49*, 1601–1622.

Talley, L. D., Rosso, I., Kamenkovich, I., Mazloff, M. R., Wang, J., Boss, E., & Sarmiento, J. L. (2019). Southern Ocean biogeochemical float deployment strategy, with example from the Greenwich Meridian line (GO-SHIP A12). *Journal of Geophysical Research: Oceans*, *124*, 403–431.

Wanninkhof, R. (2014). Relationship between wind speed and gas exchange over the ocean revisited. *Limnology and Oceanography: Methods*, *12*, 351–362.

Williams, N. L., Juranek, L. W., Feely, R. A., Johnson, K. S., Sarmiento, J. L., Talley, L. D., & Takeshita, Y. (2017). Calculating surface ocean pCO_2 from biogeochemical Argo floats equipped with pH: An uncertainty analysis. *Global Biogeochemical Cycles*, *31*, 591–604.

Williams, N. L., Juranek, L. W., Feely, R. A., Russell, J. L., Johnson, K. S., & Hales, B. (2018). Assessment of the carbonate chemistry seasonal cycles in the Southern Ocean from persistent observational platforms. *Journal of Geophysical Research: Oceans*, *123*, 4833–4852.